

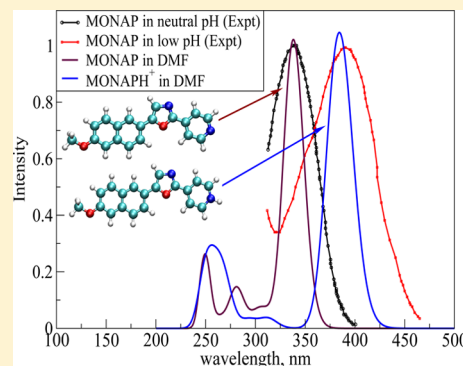
# pH-Induced Modulation of One- and Two-Photon Absorption Properties in a Naphthalene-Based Molecular Probe

N. Arul Murugan,<sup>\*,†</sup> Jacob Kongsted,<sup>‡</sup> and Hans Ågren<sup>†</sup>

<sup>†</sup>Division of Theoretical Chemistry and Biology, School of Biotechnology, Royal Institute of Technology, SE-10691 Stockholm, Sweden

<sup>‡</sup>Department of Physics, Chemistry and Pharmacy, University of Southern Denmark, Campusvej 55, DK-5230 Odense M, Denmark

**ABSTRACT:** Presently, there is a great demand for small probe molecules that can be used for two-photon excitation microscopy (TPM)-based monitoring of intracellular and intraorganelle activity and pH. The candidate molecules should ideally possess a large two-photon absorption cross section with optical properties sensitive to pH changes. In the present work, we investigate the potential of a methoxy naphthalene (MONAP) derivative for its suitability to serve as a pH sensor using TPM. Using an integrated approach rooted in hybrid quantum mechanics/molecular mechanics, the structures, dynamics, and the one- and two-photon properties of the probe in dimethylformamide solvent are studied. It is found that the protonated form is responsible for the optical property of MONAP at moderately low pH, for which the calculated pH-induced red shift is in good agreement with experiments. A 2-fold increase in the two-photon absorption cross section in the IR region of the spectrum is predicted for the moderately low pH form of the probe, suggesting that this can be a potential probe for pH monitoring of living cells. We also propose some design principles aimed at obtaining control of the absorption spectral range of the probe by structural tuning. Our work indicates that the integrated approach employed is capable of capturing the pH-induced changes in structure and optical properties of organic molecular probes and that such in silico tools can be used to draw structure–property relationships to design novel molecular probes suitable for a specific application.



## 1. INTRODUCTION

Many of the intracellular processes in the human body, such as protein synthesis, cell growth and differentiation, ion transport,<sup>1</sup> and muscle contraction, are carried out in pH-specific microenvironments.<sup>2</sup> The pH of microenvironments in different body organs has to be maintained within a characteristic range for the optimal functioning of many enzymes; for example, the functioning of salivary amylases requires a pH range between 6.5 and 7.5, whereas the gastric enzymes pepsins function in the pH range of 4–6. The pHs of different organelles, such as lysosome, cytosol, mitochondria, and golgi bodies, are kept to be around 4.7, 7.2, 8, and 6, respectively.<sup>3</sup> In addition, the pHs of body fluids are maintained in a specific range for optimal functioning. For example, the pH of blood is slightly alkaline with a pH of 7.4. There are control mechanisms in the human body that use blood, lungs, kidneys, and buffers to moderate and control the change in pH,<sup>3</sup> whereas the intraorganelles' pH is controlled by carbonic anhydrases, Na<sup>+</sup> and K<sup>+</sup> ions, and proton pumps.<sup>3</sup> Sometimes, these control mechanisms fail, leading to deviation in pH, something that is eventually associated with a number of problems and diseases, including osteoporosis, degenerative diseases, gastroesophageal reflux disease, cardiac failure and stroke, and premature aging, to mention a few examples.<sup>3,4</sup> The diagnosis of such diseases requires an intracellular or intracompartamental measurement of pH, which is a difficult and challenging task due to the in-depth

spatial location of the target structures. Currently available methods use pH microelectrodes, nuclear magnetic resonance spectrometry of metabolites, whose resonance frequency is dependent on pH, and absorption/emission of weak acid fluorescent dyes<sup>5,6</sup> and green fluorescent proteins.<sup>7–10</sup> The commonly employed one-photon microscopy is limited to cells, organs, and organelles located in close contact to the skin and is, therefore, not very useful for the intracellular pH measurements.<sup>11</sup>

To overcome these difficulties, there is a quest for molecules that can exhibit characteristic two-photon absorption/emission spectra sensitive to the pH and which, therefore, can be used to image pH in microenvironments using two-photon excitation microscopy<sup>12–14</sup> or potentially other nonlinear optical processes, as considered in ref 15. A number of probes ranging from organic molecules,<sup>16</sup> nanoparticles, and green fluorescent proteins and their mutants<sup>7,8</sup> have been proposed and shown to be successful.<sup>2</sup> Along this line, small molecular probes that can capture the pH change in the microcavities of biostructures are in demand. It would thus certainly be advantageous to establish structure–property relationships for these small molecular probes in order to come up with design strategies for a suitable molecular probe for a specific application.

Received: May 2, 2013

Published: June 24, 2013

To contribute to this subject, the present work deals with the optical properties of a recently developed small pH probe, namely, 2-methoxy-6-(5-oxazolyl) naphthalene (MONAP).<sup>4</sup> This probe has been proposed as a potential candidate for pH sensing using the TPM technique.<sup>4</sup> In this study, we explore this possibility using advanced in silico methods. This probe has previously been considered for measuring pH in, for example, living cells, the human stomach, and esophagus tissues located at 90–180  $\mu\text{m}$ .<sup>4</sup> The absorption and emission spectra of MONAP (see Figure 1a) have been studied in a number of

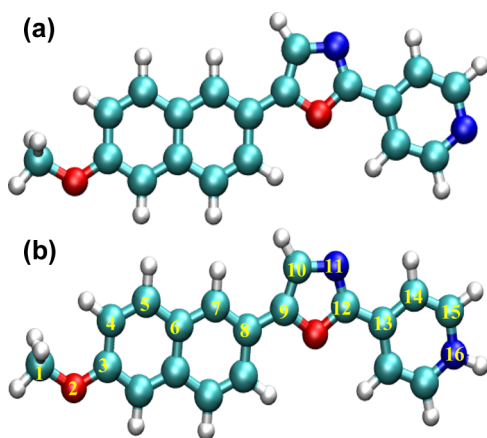


**Figure 1.** Molecular structures of (a) MONAP and (b) MONAPH<sup>+</sup>.

solvents and in HeLa cells. In a universal buffer solution, the absorption maximum of MONAP is found to be located at 342 nm, whereas the emission maximum appears at 500 nm. This corresponds to a Stokes shift of around 160 nm. This large Stokes shift has been attributed to a relatively large stabilization of the charge transfer excited state.<sup>4</sup> Moreover, with increasing solvent polarity, MONAP shows a bathochromic shift of its emission maximum, which indicates that this molecule could be used as a polarity or dielectric probe.<sup>17,18</sup> In addition, with a change in pH of the buffer solutions, the plots of  $I_{\text{blue}}/I_{\text{green}}$  (where  $I_{\text{blue}}$  and  $I_{\text{green}}$  refer to the total area of the absorption bands appearing at 300–250 and 420–470 nm, respectively) of the recorded absorption spectra have shown a remarkable pH dependence for the range of 4–6. It has been proposed that the change in absorption and emission spectra is due to the formation of a protonated form of MONAP. A suggested structure for this protonated form is shown in Figure 1b, where the nitrogen of pyridine refers to the protonation site. The current study aims to test this hypothesis. We use hybrid quantum mechanics/molecular mechanics (QM/MM)-based approaches for modeling both the structure and optical properties of MONAP and its protonated form (MONAPH<sup>+</sup>) in dimethylformamide (DMF) solvent, which mimics the intracellular dielectric environment of HeLa cells. We aim to provide insight into the mechanism for the pH-induced shift in the absorption spectra of MONAP. We also compute its two-photon absorption cross section to explore the possibility for this molecule to be used as a probe for pH sensing using the TPM technique.

Concerning modeling the pH effect, two different approaches are available: (i) an acidostat or constant pH simulations that treat the protonation states dynamically over the configurational sampling<sup>19</sup> and (ii) a static approach that employs a fixed protonation state for the molecule. The second approach is the

most popular one and is routinely used to model the pH-dependent structure of peptides and proteins. Because of its simplicity and efficiency, we have also adopted such an approach, and we use a protonated model of MONAP to study its moderately low pH optical behavior. For modeling the optical property under neutral pH, we have used MONAP in its neutral form. However, there are two nitrogen atoms available for protonation in MONAP: one in the oxazole group and another in the pyridine group (atom labels 11 and 16 of Figure 1b). The experimental  $\text{pK}_a$  values for these groups are, respectively, 0.8 and 5.1, which suggest that, at moderately low pH, the pyridine group will be the one that becomes protonated. Therefore, we use MONAP protonated at the pyridine nitrogen as a model for the moderately low pH molecular form. We study the finite temperature structures of MONAP and MONAPH<sup>+</sup> in DMF solvent using the Car–Parrinello molecular dynamics within a hybrid QM/MM framework.<sup>20–22</sup> Configurations picked up at regular intervals were used for computing the one- and two-photon absorption spectra. In particular, a polarizable QM/MM variant called the polarizable embedding (PE) scheme at the level of linear response was used for computing the one-photon absorption spectra, whereas the PE approach with quadratic response was used for the calculation of two-photon absorption cross sections. For a full description of the PE method, we refer to refs 23 and 24. To understand the importance of this dynamical averaging procedure and explicit solvent description, we also carry out property calculations for the optimized geometry of MONAP and its protonated form in DMF solvent using an implicit solvation model.

## 2. COMPUTATIONAL DETAILS

The molecular geometries of MONAP, MONAPH<sup>+</sup>, and DMF were optimized at the B3LYP/6-311++G\*\* in DMF solvent using the polarizable continuum model (PCM)<sup>25</sup> as implemented in Gaussian 09.<sup>26</sup> The partial charges for the molecules were obtained from fitting to the molecular electrostatic potential (ESP) using the CHELPG approach<sup>27</sup> as implemented in Gaussian 09. The ESP charges and the optimized molecular geometry of MONAP, MONAPH<sup>+</sup>, and DMF were used as input for the subsequent molecular dynamics simulations. The initial configurations for MONAP- and MONAPH<sup>+</sup>-solvent systems for MD were prepared by solvating a single molecule of MONAP or MONAPH<sup>+</sup> in DMF. For the latter case, we also added a  $\text{Cl}^-$  ion to neutralize the whole system. For describing the interactions between the solutes (i.e., MONAP and MONAPH<sup>+</sup>) and DMF solvent, we have used the ESP charges and the GAFF force field.<sup>28</sup> The former entities are used for describing the electrostatic interaction, whereas the latter one describes van der Waals interaction between the molecules. Molecular dynamics simulations were carried out in an orthorhombic simulation box using the Amber11 software.<sup>29</sup> For the case of MONAP, the simulation box dimensions were 53, 55, and 49 Å and the box contains one MONAP molecule and 1164 solvent molecules. In the case of MONAPH<sup>+</sup>, the dimensions were almost identical and the box included one MONAPH<sup>+</sup>, one  $\text{Cl}^-$ , and 1164 solvent molecules.

Independent of the starting configuration and density, both systems attain the correct density since the simulations were carried out within the isothermal–isobaric ensemble. The time step for the integration of the equation of motion was 1 fs, and the total simulation time was approximately 8 ns. The

Table 1. Average Bond Lengths along the Conjugation Pathway<sup>a</sup>

atom pair	static: B3LYP		static: BLYP		dynamic	
	MONAP	MONAPH <sup>+</sup>	MONAP	MONAPH <sup>+</sup>	MONAP	MONAPH <sup>+</sup>
1–2	1.43	1.43	1.45	1.45	1.46	1.46
2–3	1.36	1.36	1.38	1.37	1.38	1.38
3–4	1.42	1.42	1.43	1.43	1.43	1.42
4–5	1.38	1.38	1.39	1.39	1.38	1.38
5–6	1.42	1.42	1.43	1.43	1.43	1.43
6–7	1.41	1.41	1.42	1.42	1.42	1.42
7–8	1.39	1.39	1.40	1.40	1.40	1.40
8–9	1.45	1.45	1.46	1.45	1.46	1.46
9–10	1.37	1.38	1.38	1.40	1.38	1.39
10–11	1.38	1.37	1.39	1.37	1.38	1.38
11–12	1.30	1.31	1.32	1.33	1.31	1.32
12–13	1.46	1.44	1.46	1.44	1.46	1.45
13–14	1.40	1.41	1.41	1.42	1.41	1.42
14–15	1.39	1.37	1.40	1.38	1.39	1.38
15–16	1.34	1.35	1.36	1.37	1.35	1.36

<sup>a</sup>Results are in Å.

convergence of structural quantities such as density for both solute–solvent systems was checked for proper equilibration. The final configuration from this equilibrated MD was used as the initial configuration for the subsequent Car–Parrinello molecular dynamics in the QM/MM framework.<sup>20,21</sup> We have employed the CPMD software<sup>22</sup> interfaced<sup>30</sup> with GROMOS<sup>31</sup> for this purpose. In this run, the solvent molecules and counterion were treated using a classical force field as in the MD, whereas the solute molecules were treated at the density functional theory using the BLYP functional.<sup>32,33</sup> The wave function has been expanded in a plane-wave basis sets with an energy cutoff 80 Ry. The time step used for the integration of the equation of motion is 5 au, and a total simulation time of 30 ps has been employed for both solute–solvent systems and the reason being that the affordable time scale in a hybrid QM/MM MD or abinitio MD is limited to a few tens of picoseconds. However, care should be taken that even the low-frequency (particularly torsional) modes are sampled sufficiently during the whole simulation. In fact, we have taken care of this issue and have shown in our earlier works that such a time scale is more than sufficient to account for solute configurational sampling.<sup>34–38</sup> We first perform a quenching run to bring the solute–solvent systems to the minimum on the Born–Oppenheimer surface, which corresponds to zero temperature calculation. Furthermore, we carry out scaling and a Nose run to model the system in the finite temperature. Particularly, in the Nose run, the system is connected to a thermostat and basically samples the phase space in a canonical ensemble. The configurations picked up at regular intervals are stored for further analysis and property calculations. In particular, one- and two-photon absorption spectra calculations were performed for 75 configurations.

The one- and two-photon absorption spectra calculations for MONAP and MONAPH<sup>+</sup> were carried out using the before-mentioned PE scheme<sup>23,24</sup> implemented in a development version of DALTON2.0.<sup>39</sup> In the PE calculations, MONAP and MONAPH<sup>+</sup> were described using density functional theory employing the CAM-B3LYP<sup>40</sup> exchange–correlation functional as well as the TZVP<sup>41</sup> basis set. The solvent molecules, DMF, were described classically. The electrostatic potential fitted charges for DMF are derived at the B3LYP/aug-cc-pVTZ level of theory using the CHELPG procedure as implemented in the

Gaussian 09 software. Furthermore, the isotropic atomic polarizabilities were derived using the LoProp<sup>42</sup> approach as implemented in the MOLCAS<sup>43</sup> software. We have previously used this computational protocol for property calculations and developed polarizable force-field for the solvents and found it to provide reliable and consistent results for the optical properties of organic molecular probes involving charge transfer.<sup>34–38</sup> In addition to the dynamical calculations described above, we have also performed static calculations for the optimized structures of MONAP and MONAPH<sup>+</sup>. The level of theory for these geometry optimizations is B3LYP/6-311++G\*\* or BLYP/6-311++G\*\*, and to account for the effects of the solvent, we have used the PCM model. The cavity for the solutes was based on the UAHF model as implemented in Gaussian 09.<sup>26</sup>

### 3. RESULTS AND DISCUSSION

**3.1. pH-Induced Changes in Geometry and in Electronic Structure of the Probe.** There exists a few detailed reports on the solvent effect on the molecular structure of probe chromophores based on NMR, IR, and Raman measurements and based on theoretical calculations.<sup>44,45</sup> The usually proposed mechanism for explaining a solvent-dependent optical property of a probe is that the probe may exist in neutral, anionic, or zwitter-ionic forms depending upon the polarity of the medium, which, in turn, is responsible for dielectric sensitive changes in its absorption maximum, emission maximum, fluorescence intensity, and two-photon absorption cross sections. In some cases, the solvent effect does not entirely lead to different resonance structures but rather, to some extent, shifts the equilibrium to one or the other resonance forms. In contrast, pH effects on structural parameters of chromophores have so far not been discussed in any greater detail in the literature. Concerning the pH effects in chromophores, the molecular forms that dictate the property are rather the protonated and deprotonated forms as it has been discussed in the case of pH-sensitive green fluorescent proteins.<sup>8–10</sup> However, as such, there are no reports on the structure of moderately low and normal pH molecular forms based on neutron scattering or NMR spectroscopy. It would be useful to investigate the pH-induced change in the structure and charge distribution of the pH indicator molecules in their



sensitivity range to understand the mechanism of pH-induced changes in their properties. For this reason, we have studied the molecular conformation and the geometry along the conjugation pathway in the case of the neutral and protonated MONAP (the structure corresponding to moderately low pH). Interestingly, the protonated form remained stable during the whole QM/MM MD run and retained the proton at the nitrogen atom of the pyridine group, which suggests stability of the model chosen. The average bond length for this N–H bond was 1.03 Å, suggesting a covalent bonding between these two atoms.

We have computed the average bond lengths along the conjugation pathway for both MONAP and MONAPH<sup>+</sup> (i.e., protonated MONAP). The values are presented in Table 1 along with the bond length values obtained from the static calculations at the level of B3LYP/6-311++G\*\* as well as BLYP/6-311+G\*\*. Since the finite temperature structures from the QM/MM MD run is based on the use of the BLYP functional, in order to alone estimate the geometrical changes arising from temperature effect, the BLYP results are presented in addition to the B3LYP-based ones. By a static calculation, we mean the optimized structure of the molecule in the presence of the PCM model in order to include the effects of the DMF solvent. As it can be seen from the average bond length values reported in Table 1, the static and dynamic values appear to be comparable, suggesting that the average structure obtained from ab initio MD is not far from the values obtained based on the use of high-quality basis sets. The static results based on the BLYP functional overestimate the average bond lengths by 0.00–0.02 Å when compared to the B3LYP functional based results. The significance of these small geometrical changes with respect to the optical properties of MONAP and MONAPH<sup>+</sup> will be discussed in the next section. The structure of MONAP has almost an alternating double and single bond character along the conjugation pathway as obtained from both static and dynamic calculations. In the case of MONAPH<sup>+</sup>, the geometry remains the same as that in the deprotonated case, which reveals that the protonation does not significantly alter the geometry along the conjugation pathway.

We have also characterized the conformational geometry of MONAP and its protonated form by computing four different dihedral angles as an average over all snapshot configurations. Two of these ( $\phi_1$  and  $\phi_2$ ) are used to characterize the relative orientation of three aromatic moieties, namely, naphthalene, oxazole, and pyridine, and the third one ( $\phi_3$ ) characterizes the orientation of the methyl group carbon relative to the naphthalene group. The last one, referred to as  $\phi_4$ , has been computed to characterize the methyl group rotation dynamics. The computed value of zero for all three dihedral angles ( $\phi_1$ ,  $\phi_2$ , and  $\phi_3$ ) from the static calculations suggests a planar conformation for both MONAP and its protonated form. Even though the average values computed for  $\phi_1$  and  $\phi_2$  are close to zero, the instantaneous values were spanning the range of  $-60^\circ$  to  $+60^\circ$ , suggesting a considerable flexibility of the molecule with respect to these conformational degrees of freedom. Further, the distribution of dihedral angles  $\phi_3$  and  $\phi_4$  was spanning the angles of  $-180^\circ$  to  $180^\circ$ , suggesting a delocalized character of the associated torsional angle motion. Therefore, the dihedral angle distribution of these four angles suggests a larger conformational flexibility of MONAP and its protonated form. However, the property calculations using the optimized geometry obtained from static calculations do not account for such geometries arising from molecular flexibility. In many

optical probes, it has been shown that the sampling of the conformational degrees of freedom is important for the accurate reproduction of absorption spectra, and for this reason, the integrated approach including MD or Monte Carlo to account for configurational sampling is becoming very popular.<sup>46,47</sup> Below, we will evaluate the contribution to the absorption spectra of MONAP and its protonated form coming from such conformational flexibility.

Apart from the molecular geometry of MONAP and MONAPH<sup>+</sup>, discussed above, the charge distributions for these two systems are of relevance. In Table 2, we show the

**Table 2. Average Group Charges from Static and Dynamic Calculations<sup>a</sup>**

group	static		dynamic	
	MONAP	MONAPH <sup>+</sup>	MONAP	MONAPH <sup>+</sup>
methoxy	−0.18	−0.18	0.10	0.10
naphthalene	0.27	0.32	−0.04	0.04
oxazole	−0.04	0.06	−0.04	0.04
pyridine	−0.05	0.80	−0.02	0.82

<sup>a</sup>The static results are based on ESP charges obtained using the CHELPG procedure and calculated for the geometry optimized structure using the B3LYP functional. The set of charges termed dynamic are obtained as an average of D-RESP<sup>30</sup> charges, each calculated for a specific configuration of the solute in the solvent.

average group charges for various groups, such as methoxy, naphthalene, pyrazole, and pyridine. The pyridine group charge changes drastically between the deprotonated and the protonated molecule. However, in this case, also the static charges corresponding to the optimized geometries and the dynamic-RESP<sup>30</sup> charges from the hybrid QM/MM MD approach are comparable. Overall, we conclude that the finite temperature effect does not contribute significantly to the structure and electronic charge distribution. In contrast to what we have previously reported in the case of solvent influence on molecular geometries and charge distributions in optical probes,<sup>34,37</sup> the geometrical changes are, in this case, not very significant. However, the charge of the proton acceptor pyridine group increases to almost 0.8 from a range between  $-0.02$  and  $-0.05$ . In the case of the pH probe, the changes in geometrical parameters are thus not very significant but the charge distribution of the proton acceptor group is altered considerably.

**3.2. pH-Induced Changes in One-Photon Absorption Spectra.** Below, we discuss the one- and two-photon absorption properties of MONAP in DMF solvent, which serves as a relevant microenvironment for its use as a probe for intracellular pH measurements. As mentioned, we carry out optical property calculations using two different approaches, namely, the static and the dynamical approaches. This has been done for both the neutral and the protonated forms of MONAP. The static result is based on an optimized geometry of MONAP and MONAPH<sup>+</sup> in DMF solvent described by the PCM model. In particular, the geometries optimized using both the BLYP and the B3LYP functionals were used in the excitation energy calculations. In the excitation energy calculation, we also account for the solvent effect through PCM within a nonequilibrium solvation model. This solvation model accounts for a first-order relaxation of PCM charges with respect to the solute excited state charge distribution.

The results for the excitation energies for the six lowest transitions and the associated intensities are listed in Table 3.

**Table 3. Average Absorption Maximum (in nm) and Oscillator Strengths Associated with the Six Lowest Energy Transitions<sup>a</sup>**

excitation	MONAP	MONAPH <sup>+</sup>	shift
static calculations: B3LYP (DMF)			
1	339(1.23)	410(1.14)	71
2	307(0.05)	312(0.07)	
3	279(0.11)	301(0.01)	
4	256(0.00)	272(0.14)	
5	249(0.20)	258(0.08)	
6	246(0.24)	257(0.03)	
static calculations: BLYP (DMF)			
1	351(1.25)	429(1.18)	78
2	313(0.03)	320(0.07)	
3	286(0.09)	309(0.01)	
4	259(0.00)	278(0.13)	
5	255(0.15)	264(0.10)	
6	251(0.27)	262(0.02)	
dynamic calculations (DMF)			
1	338(1.02)	384(1.05)	46
2	306(0.07)	312(0.04)	
3	281(0.14)	294(0.03)	
4	264(0.04)	268(0.19)	
5	252(0.17)	257(0.08)	
6	246(0.16)	250(0.20)	
static calculations: B3LYP (water)			
1	338(1.20)	405(1.12)	67
2	307(0.05)	312(0.06)	
3	279(0.11)	300(0.01)	
4	256(0.00)	271(0.14)	
5	249(0.17)	257(0.07)	
6	246(0.24)	256(0.05)	
exptl <sup>4</sup>	345	398	53

<sup>a</sup>The results are shown for the static (for optimized geometries corresponding to both the BLYP and the B3LYP functionals) and dynamic calculations in DMF solvent. The static results are also shown for the case of water solvent. Experimental results for MONAP and MONAPH<sup>+</sup> have been obtained in DMF and universal buffer (pH = 2.5), respectively.<sup>4</sup>

Along with these, the dynamic results obtained from an average over various snapshots from QM/MM MD trajectory are also shown. In this case, the solvent effect is included explicitly via the PE scheme previously detailed. On the basis of the static calculations for the B3LYP-based optimized geometry, the absorption maximum corresponding to the lowest intense transition is 339 and 410 nm, respectively, for MONAP and its protonated form. This corresponds to a red shift by 71 nm in the absorption spectra. The static calculations based on the BLYP optimized geometry give results for the absorption maximum of 351 and 429 nm, respectively, predicting a red shift of 78 nm. It is relevant here to recall that, when the solution pH changes to 2.5 from neutral, the experimental absorption spectrum was red-shifted by 53 nm.<sup>4</sup> When compared to this value, the computed red shifts of 71–78 nm from the static calculations are, in fact, reasonable. The possible reasoning for this reproduction of the pH-induced shift based on the static calculations is probably associated with the

nonpolar nature of DMF and its inability to form directional hydrogen bonds with the probe, and so even a polarizable continuum model description for this solvent is sufficient. Below, we discuss the dynamic results obtained from configurational sampling. These results along with the experimental reported absorption spectra are shown in Figure 2. The calculated absorption spectra are obtained by

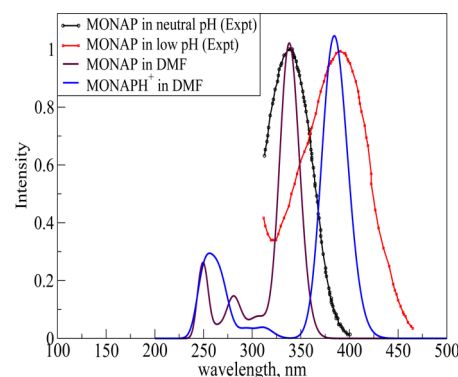


**Figure 2.** Absorption spectra of MONAP and MONAPH<sup>+</sup> in DMF solvent along with the experimentally reported spectra of MONAP under neutral and moderately low pH.

convoluting all six low-energy excitation bands as described in our previous studies.<sup>34</sup> For the line shape function width, we have not used any empirical value; rather, we have computed this from the standard deviation in the excitation energy for the particular excitation. The experimental spectra for MONAP at moderately low pH and neutral pH have both been blue-shifted by 6 nm in order to make a more visually clear comparison between the experimental and calculated results.

The absorption maximum calculated for MONAP was 338 nm, which differs from the results based on the static calculation (i.e., 351 nm based on the BLYP geometry). This suggests that the dynamical conformational changes in MONAP do contribute with some change to this excitation energy, which is in agreement with the case of, for example, *o*-betaine, where we previously reported significant contributions coming from conformational flexibility.<sup>48</sup> This statement is also true for the protonated form of MONAP where the absorption maximum computed from the dynamic calculations corresponds to 384 nm, while the static value was 429 nm, that is, a shift of 45 nm due to the conformational flexibility of the molecule. Overall, the conformational flexibility contributes significantly to the optical property of both neutral and protonated forms of MONAP and reveals the importance of conformational sampling for accurate prediction of optical property. On the basis of the dynamic calculations, the computed pH-induced shift in the absorption maximum amounts to 46 nm, which is in good agreement with the experimentally reported shift of 53 nm. The experimental absorption spectra reported for low pH and neutral pH were based on the universal buffer and DMF as media, respectively. From this, it is possible that the observed shift in the absorption spectra may also arise or have significant contributions from the change in the solvent polarity. To estimate the relative contributions due to solvent polarity and pH changes, we have carried out one more set of static calculations in water solvent for both MONAP and MONAP in its protonated form. The optimization and excitation energy calculations for MONAP and MONAPH<sup>+</sup> were performed in water solvent

described using the polarizable continuum model. The obtained results for water solvent differ only by 1–5 nm when compared to the results obtained in DMF solvent, suggesting that the shift in the optical properties has to be mostly attributed to the pH effect rather than the solvent polarity effect. This is also in complete agreement with the experimental reports on the absorption spectra of MONAP, which only shows a 2 nm shift from going from DMF to ethanol solvent.<sup>4</sup> Figures 3 and 4

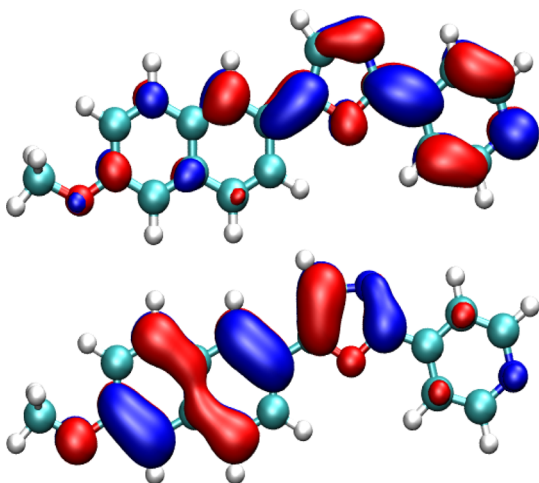


**Figure 3.** Molecular orbitals of MONAP mainly involved in the lowest energy excitation.

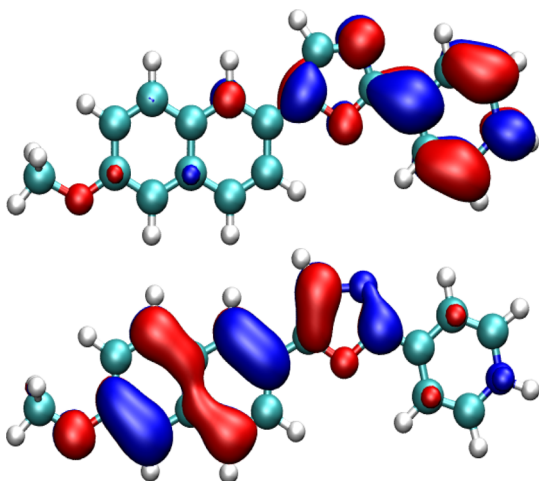


**Figure 4.** Molecular orbitals of MONAPH<sup>+</sup> mainly involved in the lowest energy excitation.

show the HOMO and LUMO orbitals of MONAP and its protonated form, which are involved in the low-energy excitation. As can be seen, this excitation involves a charge transfer from the methoxy naphthalene ring to the pyridine ring.

It is always desirable to have some insight into the structure–property relationships of probes for optimal use for a given specific application. Concerning optical probes, it is desirable to have the intense absorption band of the probe located in the near-IR region due to the possibility of penetration and reduced cell damage. For this reason, we have tried to establish a structure–property relationship based on the static calculations by changing the group connected to the naphthalene ring. We have compared the results from excitation energy calculations of MONAP and protonated MONAP with their hydroxy and trifluoromethoxy group substituted counterparts in place of the methoxy group. The latter group is known to be an electron-donating group, whereas the trifluoromethoxy group is electron-withdrawing compared to hydrogen. The results are for the optimized geometry in DMF solvent and are given in Table 4. As it can be seen, the absorption spectrum is red-shifted when an electron-donating group is connected, whereas the spectra is blue-shifted when the electron-withdrawing group is connected in the place of the hydroxy group.

**3.3. pH-Induced Changes in Two-Photon Absorption Spectra.** Next, we explore the possibility of this molecule to be used for two-photon excitation microscopy measurements<sup>13,14</sup> of intracellular pH.<sup>11</sup> This TPM methodology is most convenient concerning imaging of the intracellular pH of body organs due to the associated temporal and spatial resolution. However, the property of relevance for a probe to be used for such an application is the two-photon absorption (TPA) cross section. The molecules with TPA cross sections in the range of a few hundreds to a few thousands GM are in demand for such purposes.<sup>49,50</sup> Here, we have computed the TPA values for both MONAP and its protonated form as an average over 75 configurations from the QM/MM MD trajectory. For each such configuration, a single TPA cross section has been computed using the following expression and these intermediate results and then used to form the averaging of the TPA cross section

$$\delta_{\text{GM}} = \frac{(2\pi)^3 \alpha a_0^5 \omega^2}{c\pi\Gamma} \delta_{\text{au}} \quad (1)$$

Here,  $\alpha$  is the fine structure constant (the value is 0.0072973525),  $a_0$  is the Bohr radius (the value is 0.5291772108 Å),  $c$  is the speed of the light,  $\Gamma$  is the width of the Lorentzian-shape absorption profile, and  $\omega$  is the energy of the photon. While in most calculations,  $\Gamma$  is chosen as 0.236 eV,<sup>51,52</sup> we have demonstrated in our previous papers how to

**Table 4.** Average Absorption Maximum (in nm) and Oscillator Strengths Associated with the Four Lowest Transitions in MONAP Derivatives<sup>a</sup>

excitation	hydroxy		methoxy		trifluoromethoxy	
	neutral	protonated	neutral	protonated	neutral	protonated
1	334(1.20)	404(1.11)	339(1.23)	410(1.14)	328(1.24)	385(1.20)
2	304(0.03)	309(0.05)	307(0.05)	312(0.07)	297(0.02)	303(0.03)
3	276(0.10)	296(0.01)	279(0.11)	301(0.01)	276(0.14)	290(0.14)
4	249(0.10)	269(0.12)	249(0.20)	272(0.14)	249(0.10)	262(0.10)

<sup>a</sup>The geometry optimizations have been based on the use of B3LYP/6-311++G\*\*, and the optical properties have been calculated using CAMB3LYP/TZVP.



Table 5. Average and Maximum Two-Photon Absorption Cross Sections<sup>a</sup>

excitation	wavelength, nm	MONAP, GM	wavelength, nm	MONAPH <sup>+</sup> , GM
1	685	24(51)	764	73(160)
2	618	15(19)	623	27(31)
3	565	19(22)	587	21(22)
4	526	19(22)	533	409(600)
5	503	354(293)	513	159(231)
6	493	198(173)	499	282(424)
calcd <sub>max</sub>	700 < $\lambda$ < 900	110	700 < $\lambda$ < 900	292
exptl <sub>max</sub> <sup>4</sup>	740	155		

<sup>a</sup>Results in parentheses have been obtained using  $\Gamma = 0.236$  eV. The geometries used in these calculations are taken from the hybrid QM/MM molecular dynamics. The optical properties have been calculated using CAMB3LYP/TZVP. The results presented are an average for 75 configurations.

get this value from calculations that account for dynamics and sampling over solute–solvent configurations.<sup>38,53</sup> As in experiments, the absorption spectra are measured as an average over various snapshots, and the width of the line shape function can be computed approximately by evaluating the standard deviation of the excitation energy (i.e.,  $\Gamma \approx 0.23548\sigma$ ). Therefore, we have computed the TPA cross section values using the  $\Gamma$  computed from simulation as well as using the standard value of 0.236 eV.<sup>51</sup> Both values computed for both molecules (MONAP and its protonated form) for the six lowest energy excitations are given in Table 5. The results based on  $\Gamma = 0.236$  eV are given in parentheses. Along with these values, we have also presented the maximum value for the computed TPA cross sections for the excitation energy range of 700–900 nm. Because the radiation in the near-IR and IR regions is less harmful and can penetrate deeper, this spectral range is highly relevant in the context of living cell imaging. In addition, the computed TPA cross section values for all configurations are presented as a scatter diagram in Figure 5 (with  $x$

standard  $\Gamma$  and ab initio  $\Gamma$  differ significantly for the first low-energy band, and in particular, the TPA values predicted from standard  $\Gamma$  are 2-fold larger than the counterpart. As seen in Table 5, the first band for MONAP and MONAPH<sup>+</sup> is not so intense with respect to two-photon absorption but is the most relevant one since the excitation energy wavelength is in either the near-IR or the IR region. The computed average TPA value of MONAP for this excitation is 24 GM. The computed TPA<sub>max</sub> is 103 GM compared with the experimental reported value of 155 GM. The computed average TPA value for the first excitation is almost 3-fold times larger (i.e., 70 GM) for the protonated form when compared to the neutral form. The trend remains the same even for the TPA calculated using standard  $\Gamma$ . Interestingly, for MONAP and its protonated form, the two-photon absorption processes associated with higher intensity appear in the frequency range < 530 nm.

Overall, the TPA values for the protonated form are larger when compared to the neutral form. Such an increase in the TPA intensity and its pH dependence of the absorption maximum clearly suggest that this molecule can be used as a potential probe for pH measurements based on one- and two-photon microscopy techniques. In addition, the relatively small size of this probe when compared to, for example, GFPs is advantageous for intracellular and intraorganelle pH measurements. We also show that the scanning range of the spectrum can be tuned by adopting some structural changes within the probe. The reason for such an above-discussed increase in TPA values for the protonated form when compared to the neutral form can be rationalized using the two-state model (2SM) for the TPA cross sections, which is given below

$$\delta^{2SM} = \frac{16}{15} \frac{|\mu^{01}|^2 |\Delta\mu|^2}{\omega^2} (1 + 2 \cos^2 \theta_{\Delta\mu}^{01}) \quad (2)$$

Here,  $\mu^{01}$  and  $\Delta\mu$  refer to the transition dipole from the ground to the first excited state and the difference between the excited and ground state dipole moments, respectively. The  $\theta_{\Delta\mu}^{01}$  refers to the angle between these two vectors, while the  $\omega$  refers to the excitation energy. The values of these four parameters involved in the two-state model are presented in Table 6. The calculations were performed for the optimized geometries of MONAP and its protonated form in DMF solvent described using the PCM model. As it can be seen, the 2SM predicted values and the response theory average values are in fairly good agreement for this lowest energy transition. The 2SM predicted TPA values for MONAP and its protonated form are, respectively,  $18 \times 10^3$  and  $117 \times 10^3$  au, which are in reasonable agreement with the configurations averaged TPA

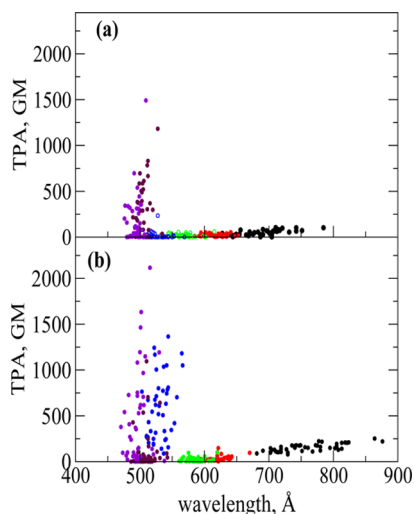


Figure 5. Scatter diagrams of excitation energy and TPA values for the six lowest energy excitations: (a) MONAP and (b) MONAPH<sup>+</sup>.

corresponding to half the energy of a photon and  $y$  corresponding to the TPA value computed using  $\Gamma = 0.236$  eV). Since the maximum of TPA cross sections often is reported in experiments for the sake of comparison, the TPA<sub>max</sub> from Figure 5 is also given in Table 5 (only for the wavelength range around and closer to the IR region and, in particular, >700 nm). As seen, the average values computed using

Table 6. Two-State Model Analysis Parameters<sup>a</sup>

system	$\mu^{01}$	$\Delta\mu$	$\theta_{\Delta\mu}^{01}$	$\omega$	$\delta^{2SM} \times 10^3$
MONAP	3.708	2.758	176.04	0.135	18.27 (14.87)
MONAPH <sup>+</sup>	3.899	5.615	177.27	0.114	117.24 (51.26)

<sup>a</sup>All numbers are reported in au. The calculations are performed for the geometries of MONAP and MONAPH<sup>+</sup> optimized using the B3LYP functional. The numbers in parenthesis refer to the average values from response theory calculations.

values of  $15 \times 10^3$  and  $51 \times 10^3$  au. The two-state model clearly explains the pH-induced increase in the TPA values of MONAP. As we can see from Table 6, even though the transition dipole moments ( $\mu^{01}$ ) for both the neutral and the protonated forms are comparable, for the latter, there is a substantial (2-fold) increase in the difference between the ground and excited state dipole moments. It is also worthwhile to note that the transition dipole moment vector and difference vector of excited and ground state dipole moments align in parallel (i.e., the angles are almost closer to  $180^\circ$ ) to yield the increased TPA values for both MONAP and its protonated form.

Finally, we also investigated for any potential correlation between the two-photon cross sections and the spatial overlap of the occupied and virtual molecular orbitals involved in the excitation. The spatial overlap (referred to as  $\Lambda$ ) carries a value between 0 and 1 to describe the nature of the excitation: a large value for  $\Lambda$  indicates a large overlap between the occupied and virtual orbitals involved in the particular excitation process and suggests a local nature of the excitation, whereas a small value for  $\Lambda$  indicates a long-range charge transfer excitation. This has been discussed as a diagnostic parameter in relevance to the judicious use of different density functionals in describing transitions with large charge transfer character.<sup>54</sup> More recently, its connection to the two-photon absorption cross section in a intermolecular charge transfer complex has been discussed in some detail,<sup>52</sup> which suggests that a decrease in  $\Lambda$  is related to an increase in the TPA value. Recently, another study showed a correlation between the spatial overlap and the difference between the ground and excited state molecular dipole moments.<sup>55</sup> In fact, this also suggests that a small value of  $\Lambda$  is to be associated with larger differences in dipole moments and so suggests again an increased TPA.<sup>55</sup> We will here examine whether there is any correlation between  $\Lambda$  and the TPA values for both MONAP and its protonated form. Above, we have discussed that the first excitation in the case of MONAP and its protonated form has intramolecular charge transfer character (refer to the HOMO, LUMO molecular orbitals involved in the excitation). Therefore, we have restricted this analysis to the lowest energy transition. The results are presented for both MONAP and its protonated form as a scatter diagram (with  $x$  referring to spatial overlap,  $\Lambda$  and  $y$  referring to TPA cross sections) in Figure 6. The average TPA values for the given range of  $\Lambda$  (with bin value of 0.05 for the spatial overlap) are also shown in the plot. It shows that, in fact, there is a fairly linear relationship between  $\Lambda$  and the TPA cross sections. A smaller  $\Lambda$  is seen in the case of MONAPH<sup>+</sup>, and this, in fact, has comparably larger TPA values. In contrast, MONAP, which, in turn, has larger  $\Lambda$  values, is associated with smaller TPA values (see Figure 6). This can be explained due to the fact that a decrease in  $\Lambda$  leads to an increase in the difference between the excited and ground state dipole moments, which appears in the numerator of the 2SM

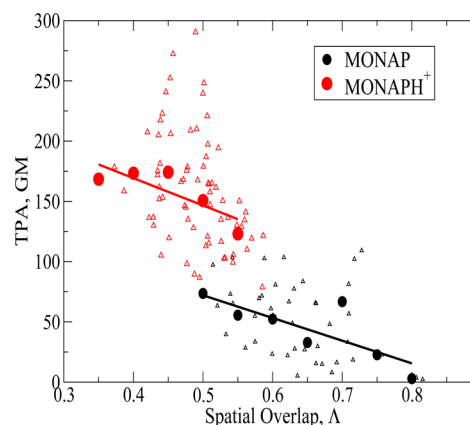


Figure 6. Scatter diagram of TPA values and spatial overlap for 75 instantaneous configurations of MONAP and MONAPH<sup>+</sup>. The plot also shows averaged values of TPA for a range of  $\Lambda$ , between  $x$  and  $x + 0.05$ . A linear fitting for the two sets of averaged values is also shown in this figure.

expression and thereby contributes to the increase in TPA values. From this, we conclude that the TPA values of MONAP and its protonated form can be tuned by suitably altering the charge transfer character within the system, which can be achieved with substitution of electron-donating and withdrawing-groups in the appropriate places in the conjugation pathway.

#### 4. CONCLUSIONS

We have studied the pH-dependent structure, dynamics, and one- and two-photon absorption properties of a naphthalene-based probe. The molecular structure protonated at the pyridine nitrogen site is shown to be responsible for the moderately low pH behavior of the probe. While the protonation process does not alter the molecular geometry with respect to the conjugation pathway and conformation geometry, the charge distribution in the pyridine ring is significantly altered. Static calculations appear to be sufficient to reproduce the structure and absorption properties of the probe under neutral pH. However, it becomes important to account for the conformational sampling to accurately reproduce the moderately low pH properties of the probe. The adopted integrated approach could successfully reproduce the absorption spectra of the probe in moderately low and neutral pH and also the pH-induced red shift in the spectra in excellent agreement with experimental spectra. We also reported a pH-induced 2-fold increase in the TPA values for the probe, which, in fact, suggests that this can be a potential probe to monitor pH changes. On the basis of the two-state model, we explain that the difference between the excited and the ground state dipole moments is the main responsible factor for the increased TPA value associated with the moderately low pH form. We also identify that there exists a correlation between the spatial overlap and TPA values corresponding to the lowest energy excitation having charge transfer character. Because the results are obtained for the probe in DMF solvent, which mimics the intracellular environment in HeLa cells, we suggest that this probe can be used for monitoring intracellular pH changes.

#### ■ AUTHOR INFORMATION

##### Corresponding Author

\*E-mail: murugan@theochem.kth.se.



## Notes

The authors declare no competing financial interest.

## ACKNOWLEDGMENTS

This work was supported by a grant from the Swedish Infrastructure Committee (SNIC) for the project "Multiphysics Modeling of Molecular Materials", SNIC 023/07-18. J.K. thanks the Danish Center for Scientific Computing (DCSC), The Danish Councils for Independent Research (The Sapere Aude programme), the Lundbeck Foundation, and the Villum Foundation for financial support.

## REFERENCES

- (1) Boron, W. F. *Annu. Rev. Physiol.* **1986**, *48*, 377–388.
- (2) Han, J.; Burgess, K. *Chem. Rev.* **2010**, *110*, 2709–2728.
- (3) Casey, J. R.; Grinstein, S.; Orlowski, J. *Nat. Rev. Mol. Cell Biol.* **2010**, *11*, 50–61.
- (4) Park, H. J.; Lim, C. S.; Kim, E. S.; Han, J. H.; Lee, T. H.; Chun, H. J.; Cho, B. R. *Angew. Chem., Int. Ed.* **2012**, *51*, 2673–2676.
- (5) Kurkdjian, A.; Guern, J. *Annu. Rev. Plant Physiol. Plant Mol. Biol.* **1989**, *40*, 271–303.
- (6) Nuccitelli, R.; Deamer, D. W., Eds. *Intracellular pH: Its Measurement, Regulation and Utilization in Cellular Functions*; Liss: New York, 1982; p 594.
- (7) Battisti, A.; Digman, M. A.; Gratton, E.; Storti, B.; Beltrama, F.; Bizzarri, R. *Chem. Commun.* **2012**, *48*, 5127–5129.
- (8) Bizzarri, R.; Serresi, M.; Luin, S.; Beltram, F. *Anal. Bioanal. Chem.* **2009**, *393*, 1107–1122.
- (9) Miesenböck, G.; De Angelis, D. A.; Rothman, J. E. *Nature* **1998**, *394*, 192–195.
- (10) Zimmer, M. *Chem. Rev.* **2002**, *102*, 759–782.
- (11) Roos, A.; Boron, W. F. *Physiol. Rev.* **1981**, *61*, 296–434.
- (12) Denk, W.; Strickler, J.; Webb, W. *Science* **1990**, *248*, 73–76.
- (13) Imanishi, Y.; Lodowski, K. H.; Koutalos, Y. *Biochemistry* **2007**, *46*, 9674–9684.
- (14) Zoumi, A.; Yeh, A.; Tromberg, B. J. *Proc. Natl. Acad. Sci. U.S.A.* **2002**, *99*, 11014–11019.
- (15) Asselberghs, I.; Flors, C.; Ferrighi, L.; Botek, E.; Champagne, B.; Mizuno, H.; Ando, R.; Miyawaki, A.; Hofkens, J.; Van der Auweraer, M.; Clays, K. *J. Am. Chem. Soc.* **2008**, *130*, 15713–15719.
- (16) Huang, R.; Yan, S.; Zheng, X.; Luo, F.; Deng, D.; Fu, B.; Xiao, Y.; Zhao, X.; Zhou, X. *Analyst* **2012**, *137*, 4418–4420.
- (17) Reichardt, C. *Chem. Rev.* **1994**, *94*, 2319–2358.
- (18) Katritzky, A. R.; Fara, D. C.; Yang, H.; Tamm, K.; Tamm, T.; Karelson, M. *Chem. Rev.* **2004**, *104*, 175–198.
- (19) Machuqueiro, M.; Baptist, A. M. *J. Phys. Chem. B* **2006**, *110*, 2927–2933.
- (20) Warshel, A.; Levit, M. *J. Mol. Biol.* **1976**, *103*, 227–249.
- (21) Field, M. J.; Bash, P. A.; Karplus, M. *J. Comput. Chem.* **1990**, *11*, 700–733.
- (22) Hutter, J.; Parrinello, M.; Marx, D.; Focher, P.; Tuckerman, M.; Andreoni, W.; Curioni, A.; Fois, E.; Röthlisberger, U.; Giannozzi, P.; Deutsch, T.; Alavi, A.; Sebastiani, D.; Laio, A.; VandeVondele, J.; Seitsonen, A.; Billeter, S. *Computer Code CPMD*, version 3.11; IBM Corp.: Stuttgart, Germany, 1990–2008 and MPI-FKF: Stuttgart, Germany, 1997–2001.
- (23) Olsen, J. M. H.; Aidas, K.; Kongsted, J. *J. Chem. Theory Comput.* **2010**, *6*, 3721–3734.
- (24) Olsen, J. M. H.; Kongsted, J. *Adv. Quantum Chem.* **2011**, *61*, 107–143.
- (25) Tomasi, J.; Mennucci, B.; Cammi, R. *Chem. Rev.* **2005**, *105*, 2999–3094.
- (26) Frisch, M. J.; Trucks, G. W.; Schlegel, H. B.; Scuseria, G. E.; Robb, M. A.; Cheeseman, J. R.; Scalmani, G.; Barone, V.; Mennucci, B.; Petersson, G. A.; Nakatsuji, H.; Caricato, M.; Li, X.; Hratchian, H. P.; Izmaylov, A. F.; Bloino, J.; Zheng, G.; Sonnenberg, J. L.; Hada, M.; Ehara, M.; Toyota, K.; Fukuda, R.; Hasegawa, J.; Ishida, M.; Nakajima, T.; Honda, Y.; Kitao, O.; Nakai, H.; Vreven, T.; Montgomery, J. A., Jr.; Peralta, J. E.; Ogliaro, F.; Bearpark, M.; Heyd, J. J.; Brothers, E.; Kudin, K. N.; Staroverov, V. N.; Kobayashi, R.; Normand, J.; Raghavachari, K.; Rendell, A.; Burant, J. C.; Iyengar, S. S.; Tomasi, J.; Cossi, M.; Rega, N.; Millam, J. M.; Klene, M.; Knox, J. E.; Cross, J. B.; Bakken, V.; Adamo, C.; Jaramillo, J.; Gomperts, R.; Stratmann, R. E.; Yazyev, O.; Austin, A. J.; Cammi, R.; Pomelli, C.; Ochterski, J. W.; Martin, R. L.; Morokuma, K.; Zakrzewski, V. G.; Voth, G. A.; Salvador, P.; Dannenberg, J. J.; Dapprich, S.; Daniels, A. D.; Farkas, Ö.; Foresman, J. B.; Ortiz, J. V.; Cioslowski, J.; Fox, D. J. *Gaussian 09*, Revision A.02; Gaussian Inc.: Wallingford, CT, 2009.
- (27) Breneman, C. M.; Wiberg, K. B. *J. Comput. Chem.* **1990**, *11*, 361–373.
- (28) Wang, J.; Wolf, R. M.; Caldwell, J. W.; Kollman, P. A.; Case, D. A. *J. Comput. Chem.* **2004**, *25*, 1157–1174.
- (29) Case, D. A.; Darden, T. A.; Cheatham, T. E., III; Simmerling, C. L.; Wang, J.; Duke, R. E.; Luo, R.; Walker, R. C.; Zhang, W.; Merz, K. M.; Roberts, R.; Wang, B.; Hayik, S.; Roitberg, A.; Seabra, G.; Kolossváry, I.; Wong, K. F.; Paesani, F.; Vanicek, J.; Liu, J.; Wu, X.; Brozell, S. R.; Steinbrecher, T.; Gohlke, H.; Cai, Q.; Ye, X.; Wang, J.; Hsieh, M.-J.; Cui, G.; Roe, D. R.; Mathews, D. H.; Seetin, M. G.; Sagui, C.; Babin, V.; Luchko, T.; Gusarov, S.; Kovalenko, A.; Kollman, P. A. *AMBER 11*; University of California: San Francisco, 2010.
- (30) Laio, A.; VandeVondele, J.; Röthlisberger, U. *J. Phys. Chem. B* **2002**, *106*, 7300–7307.
- (31) van Gunsteren, W. F.; Billeter, S. R.; Eising, A. A.; Hünenberger, P. H.; Krüger, P.; Mark, A. E.; Scott, W. R. P.; Tironi, I. G. *Biomolecular Simulation: The GROMOS96 Manual and User Guide*; Vdf Hochschulverlag AG an der ETH Zürich: Zürich, 1996.
- (32) Becke, A. D. *Phys. Rev. A* **1988**, *38*, 3098–3100.
- (33) Lee, C.; Yang, W.; Parr, R. C. *Phys. Rev. B* **1988**, *37*, 785–789.
- (34) Murugan, N. A.; Kongsted, J.; Rinkevicius, Z.; Ågren, H. *Proc. Natl. Acad. Sci. U.S.A.* **2010**, *107*, 16453–16458.
- (35) Murugan, N. A.; Olsen, J. M. H.; Kongsted, J.; Rinkevicius, Z.; Aidas, K.; Ågren, H. *J. Phys. Chem. Lett.* **2013**, *4*, 70–77.
- (36) Murugan, N. A.; Aidas, K.; Kongsted, J.; Rinkevicius, Z.; Ågren, H. *Chem.—Eur. J.* **2012**, *18*, 11677–11684.
- (37) Murugan, N. A.; Kongsted, J.; Rinkevicius, Z.; Ågren, H. *Phys. Chem. Chem. Phys.* **2012**, *14*, 1107–1112.
- (38) Murugan, N. A.; Kongsted, J.; Zilvinas, R.; Aidas, K.; Mikkelsen, K.; Ågren, H. *Phys. Chem. Chem. Phys.* **2011**, *13*, 12506–12516.
- (39) DALTON: A Molecular Electronic Structure Program, release 2.0 edition; 2005. See: <http://www.kjemi.uio.no/software/dalton/dalton.html>.
- (40) Yanai, T.; Tew, D. P.; Handy, N. C. *Chem. Phys. Lett.* **2004**, *393*, 51–57.
- (41) Schäfer, A.; Huber, C.; Ahlrichs, R. *J. Chem. Phys.* **1994**, *100*, 5829.
- (42) Gagliardi, L.; Lindh, R.; Karlström, G. *J. Chem. Phys.* **2004**, *121*, 4494.
- (43) Aquilante, F.; De Vico, L.; Ferré, N.; Ghigo, G.; Malmqvist, P.-Å.; Neogrády, P.; Pedersen, T. B.; Pitoňák, M.; Reiher, M.; Roos, B. O.; Serrano-Andrés, L.; Urban, M.; Veryazov, V.; Lindh, R. *J. Comput. Chem.* **2010**, *31*, 224–247.
- (44) Mustroph, H.; Mistol, J.; Senns, B.; Keil, D.; Findeisen, M.; Hennig, L. *Angew. Chem., Int. Ed.* **2009**, *48*, 8773.
- (45) Yamaguchi, T.; Kimura, Y.; Hirota, N. *J. Phys. Chem. A* **1997**, *101*, 9050–9060.
- (46) Barone, V.; Baiardi, A.; Biczysko, M.; Bloino, J.; Cappelli, C.; Lipparini, F. *Phys. Chem. Chem. Phys.* **2012**, *14*, 12404–12422.
- (47) Zazza, C.; Coletta, A.; Sanna, N.; Chillemi, G.; Mancini, G.; Desideri, A. *J. Phys. Chem. B* **2010**, *114*, 6770–6778.
- (48) Murugan, N. A.; Ågren, H. *J. Phys. Chem. A* **2009**, *113*, 2572–2577.
- (49) Albota, M.; Beljonne, D.; Bredas, J.-L.; Ehrlich, J. E.; Fu, J. Y.; Heikal, A. A.; Hess, S. E.; Kogej, T.; Levin, M. D.; Marder, S. R.; Maughon, D. M.; Perry, J. W.; Röckel, H.; Rumi, M.; Subramaniam, G.; Webb, W. W.; Wu, X.-L.; Xu, C. *Science* **1998**, *281*, 1653–1656.
- (50) He, G. S.; Tan, L.-S.; Zheng, Q.; Prasad, P. N. *Chem. Rev.* **2008**, *108*, 1245–1330.

- (51) Day, P. N.; Nguyen, K. A.; Pachter, R. J. *Phys. Chem. B* **2005**, *109*, 1803–1814.
- (52) Chakrabarti, S.; Ruud, K. *Phys. Chem. Chem. Phys.* **2009**, *11*, 2592–2596.
- (53) Silva, D. L.; Murugan, N. A.; Kongsted, J.; Rinkevicius, J.; Canuto, S.; Ågren, H. J. *Phys. Chem. B* **2012**, *116*, 8169–8181.
- (54) Peach, M. J. G.; Benfield, P.; Helgaker, T.; Tozer, D. J. *J. Chem. Phys.* **2008**, *128*, 044118.
- (55) Eriksen, J. J.; Sauer, S. P. A.; Mikkelsen, K. V.; Christiansen, O.; Jensen, H. J. A.; Kongsted, J. *Mol. Phys.* **2013**, DOI: 10.1080/00268976.2013.793841.